Biophysical Journal, Volume *120*

Supplemental information

Chemotactic migration of bacteria in porous media

Tapomoy Bhattacharjee, Daniel B. Amchin, Jenna A. Ott, Felix Kratz, and Sujit S. Datta

Supplementary Information for

Chemotactic Migration of Bacteria in Porous Media

T. Bhattacharjee[†], D. B. Amchin[†], J. A. Ott, F. Kratz & S. S. Datta*

[†]*These authors contributed equally to this work.*

*Email: ssdatta@princeton.edu

Supplementary Movie Captions

Movie S1 (separate file): Bottom-up view of chemotactic migration in media with largest pores. Maximum intensity projection of chemotactic migration from a cylinder of close-packed *E. coli* 3D-printed within a medium with a = 2.2 μm.

Movie S2 (separate file): End-on view of chemotactic migration in media with largest pores. Maximum intensity projection of chemotactic migration from a cylinder of close-packed *E. coli* 3D-printed within a medium with a = 2.2 μm.

Movie S3 (separate file): Single cell hopping and trapping at the leading edge of a propagating front. Bottom-up imaging of cells at the leading edge of a front propagating in a medium with a = 2.2 μm; direction of front propagation is upward.

Movie S4 (separate file): Bottom-up view of chemotactic migration in media with medium sized pores. Maximum intensity projection of chemotactic migration from a cylinder of close-packed *E. coli* 3D-printed within a medium with a = 1.7 μm.

Movie S5 (separate file): End-on view of chemotactic migration in media with medium sized pores. Maximum intensity projection of chemotactic migration from a cylinder of close-packed *E. coli* 3D-printed within a medium with a = 1.7 μm.

Movie S6 (separate file): Bottom-up view of chemotactic migration in media with smallest pores. Maximum intensity projection of chemotactic migration from a cylinder of close-packed *E. coli* 3D-printed within a medium with a = 1.2 μm.

Movie S7 (separate file): End-on view of chemotactic migration in media with smallest pores. Maximum intensity projection of chemotactic migration from a cylinder of close-packed *E. coli* 3D-printed within a medium with a = 1.2 μm.

Movie S8 (separate file): Cell-cell collisions truncate hopping. Bottom-up imaging of two cells of *E. coli* colliding within a porous medium. The cell bodies are shown in green, and the fluorescently-labeled flagella, which help determine the orientation of the moving cell, are shown in magenta. One cell (initially in the top right) is moving along a hop in the pore space, while the other (middle) is trapped for the duration of the movie. The moving cell eventually collides with the initially trapped cell, which causes it to become transiently trapped itself, until it can eventually reorient and continue to move through the pore space. Thus, this cell-cell interaction truncates the hopping length of the moving cell. In this experiment, cells are dispersed in a medium with a = 3.6 μm swollen in liquid LB, and flagella are labelled using Alexa Fluor dye, as detailed in our previous work (Ref. 14).

Movie S9 (separate file): Cell-cell collisions truncate hopping in a migrating front, and cell swimming does not appreciably deform the solid matrix. Bottom-up imaging of cells within a front propagating in a porous medium to the left, imaged > 4h after 3D-printing the initial cylindrical inoculum. Moving cells collide with each other due to crowding, truncating each other's hopping; however, we do not observe any other cooperative motions. Furthermore, a number of trapped cells act as tracers of matrix deformations; they do not move noticeably, even as neighboring cells migrate by, indicating that the solid matrix is not appreciably deformed by cell swimming. In this

experiment, the medium has a = 3.6 μm swollen in liquid LB, with properties detailed in our previous work (Ref. 14).

Movie S10 (separate file): Numerical simulation of chemotactic migration in media with largest pores. Numerical simulations of cellular signal (blue lines) and nutrient concentration (red lines), normalized by maximal initial value, for different radial positions and at different times, for a medium with a = 2.2 μm.

Movie S11 (separate file): Numerical simulation of chemotactic migration in media with medium sized pores. Numerical simulations of cellular signal (blue lines) and nutrient concentration (red lines), normalized by maximal initial value, for different radial positions and at different times, for a medium with a = 1.7 μm.

Movie S12 (separate file): Numerical simulation of chemotactic migration in media with smallest pores. Numerical simulations of cellular signal (blue lines) and nutrient concentration (red lines), normalized by maximal initial value, for different radial positions and at different times, for a medium with a = 1.2 μm.

Movie S13 (separate file): End-on view of chemotactic migration from two closely-spaced cylindrical populations. Maximum intensity projection of chemotactic migration from two cylinders of close-packed *E. coli* 3D-printed within a medium with a = 1.7 μm and with axes separated by 0.5 mm. Chemotactic fronts only move outward, not inward between the cylinders.

Movie S14 (separate file): End-on view of chemotactic migration from two well-spaced cylindrical populations. Maximum intensity projection of chemotactic migration from two cylinders of close-packed *E. coli* 3D-printed within a medium with a = 1.7 μm and with axes

separated by 5 mm. Chemotactic fronts move both outward and inward between the cylinders.

Movie S15 (separate file): Numerical simulation of oxygen levels during chemotactic migration in media with medium size pores. Numerical simulations of cellular signal (blue lines) and oxygen concentration (red lines), normalized by maximal initial value, for different radial positions and at different times, for a medium with a = 1.7 μm. The resulting oxygen profile is qualitatively similar to the nutrient profile shown in Movie S9. Both oxygen and nutrient are depleted behind the front, supporting our expectation that the front contains aerobically metabolically active cells while behind the front cells are starved.

Movie S16 (separate file): Numerical simulation of chemotactic migration in media with medium size pores, with initial nutrient depletion. Numerical simulations of cellular signal (blue lines) and nutrient concentration (red lines), normalized by maximal initial value, for different radial positions and at different times, for a medium with a = 1.7 μm. In this case, the nutrient is not saturated everywhere initially, but is instead depleted within the initial population; however, we find identical results to the case with nutrient saturated everywhere.

Supplementary Figures

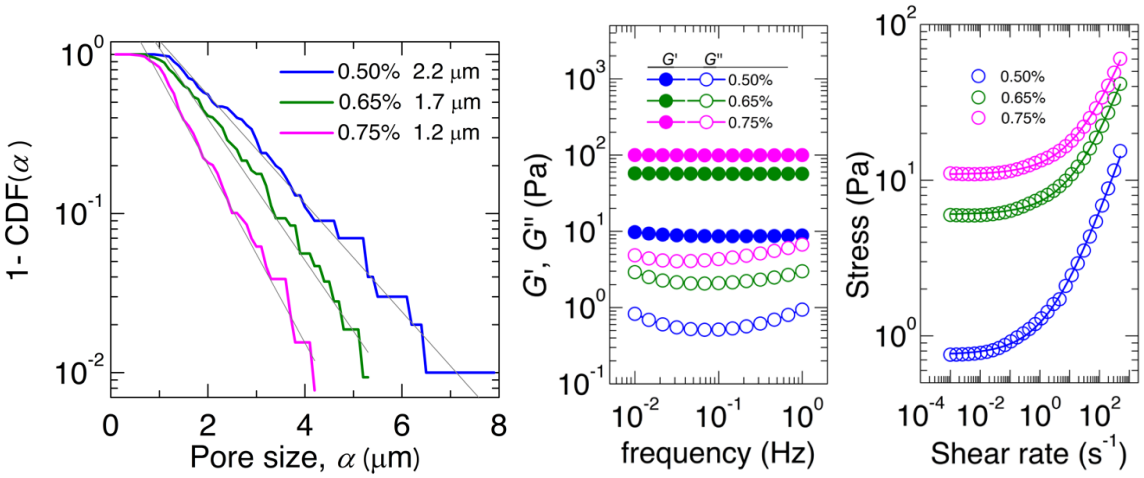

Figure S1. Characterization of porous media. (Left) Using measurements of many different tracers, which obtain the complementary cumulative distribution function 1-CDF($\boldsymbol{\alpha}$) for each of the three porous media; here, CDF($\boldsymbol{\alpha}$) $\equiv \sum_0^{\alpha} \boldsymbol{\alpha}\boldsymbol{\rho}(\boldsymbol{\alpha}) / \sum_0^{\infty} \boldsymbol{\alpha}\boldsymbol{\rho}(\boldsymbol{\alpha})$ and $\boldsymbol{\rho}(\boldsymbol{\alpha})$ is the number fraction of pores having dimension $\boldsymbol{\alpha}$. To determine the mean pore size, we fit an exponential $\sim \boldsymbol{e}^{-\alpha/A}$ to 1-CDF($\boldsymbol{\alpha}$) for each medium and report the mean pore size as $\boldsymbol{a} = \boldsymbol{A} + \boldsymbol{\alpha_0}$ where $\boldsymbol{\alpha_0}$ is the largest pore size with CDF = 0. **(Middle)** Small-amplitude measurements of elastic (closed symbols) and viscous (open symbols) shear moduli, *G'* and *G''* respectively, of the porous media at different oscillatory frequencies. The legend indicates the hydrogel mass fraction used to prepare the media. The elastic moduli are frequency independent and are larger than the viscous moduli, indicating that the porous media are elastic solids. **(Right)** Measurements of shear stress as a function of applied unidirectional shear rate. At low shear rates the porous media behave like elastic solids with a yield stress given by the low shear rate asymptote of the curves shown; at high shear rates the media become fluidized.

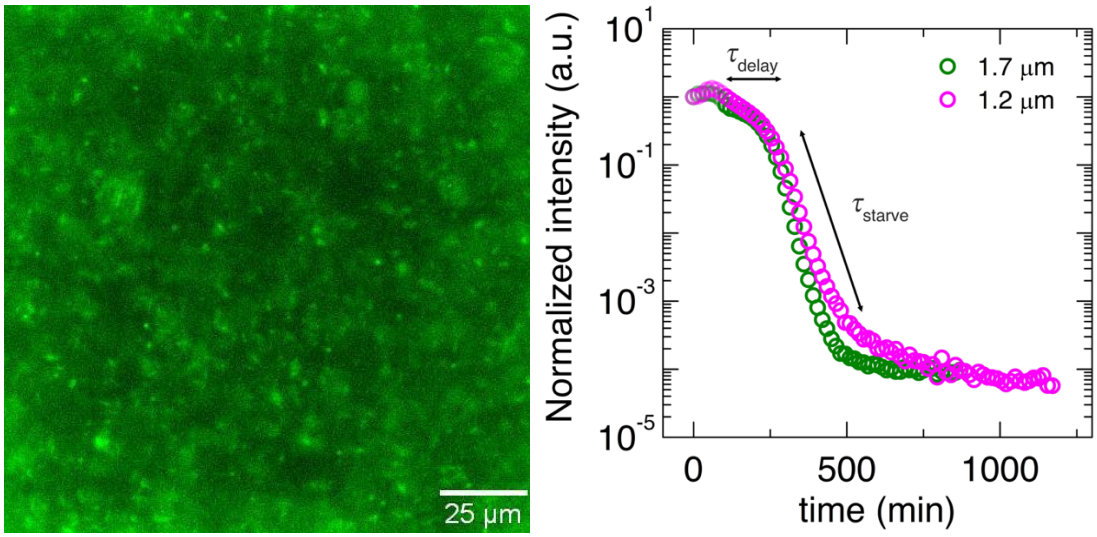

Figure S2: Oxygen-depleted cells remain trapped in initial position and eventually lose fluorescence. (Left) Fluorescence micrograph of cells trapped at the initial position of a cylindrical population ~17 h after 3D printing, well after front formation and propagation away. The cells are nonmotile and lose fluorescence; this image was taken by increasing the excitation intensity by ~29 times than used in all other experiments. **(Right)** Total fluorescence intensity measured at the center of a cylindrical population, normalized by initial intensity, in two different porous media with different mean pore sizes, indicated by the legend. Initially the cells migrate radially outward, leading to an initial slight decrease in fluorescent intensity (light symbols). The cells that remain trapped in their initial position maintain fluorescence for $\boldsymbol{\tau_{delay}}$ = 2 h and then lose fluorescence over a time scale of $\boldsymbol{\tau_{starve}}$ = 29.7 min, which likely reflects oxygen deprivation since the GFP that enables cells to be fluorescent requires oxygen to properly fold.

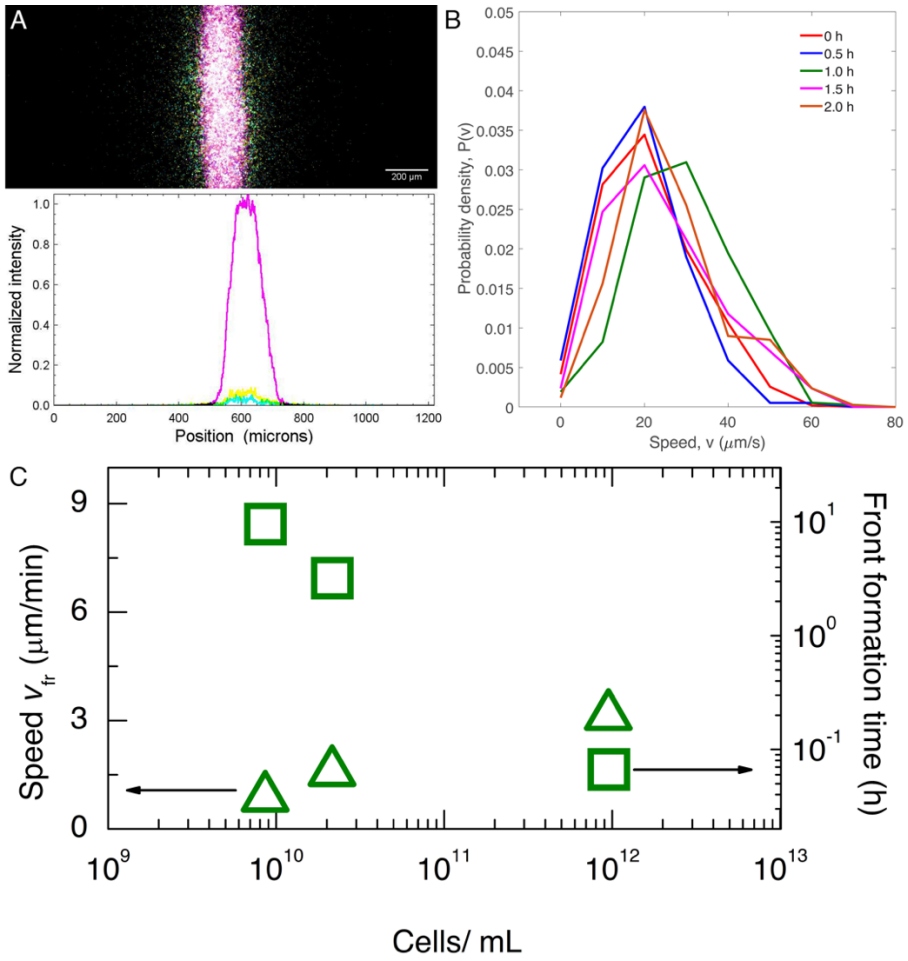

Figure S3: Front propagation is modulated by nutrient consumption. (A) Fronts do not form without nutrient. We 3D-print a cylinder of dense-packed *E. coli* within a medium prepared using 0.75% mass fraction hydrogel swollen in nutrient-free M9 minimal media instead of nutrient-rich EZ Rich media. We find that the population spreads outward diffusively, but does not form fronts, over the time scale required for fronts to form in nutrient-rich media (magenta: 0 h, yellow: 1 h, cyan: 2 h) – even though the cells remain motile over this time scale (since the edge of the population is not oxygen-depleted), corroborated by the data in panel B, consistent with previous studies indicating that *E. coli* remains motile without nutrients, powered by their endogenous metabolism, over this time scale (e.g., Refs. 90-91). Thus, when nutrient is present, consumption by the cells generates the local gradient that they in turn bias their motion along – an essential requirement for chemotactic migration. Left panel shows bottom-up fluorescence micrograph of the population as it spreads, while right panel shows normalized intensity profiles through the 3D-printed population. **(B)** Distributions of instantaneous swimming speed of cells in bulk nutrient-free M9 minimal liquid media. **(C)** Front formation takes longer in more dilute populations. Data for a cylindrical population 3D-printed at different initial cell densities (horizontal axis) in a medium with a = 1.7 μm. The left vertical axis indicates the long-time speed of the propagating front formed $\boldsymbol{v_{fr}}$, while the right vertical axis indicates the front formation time measured by monitoring when the fluorescence intensity measured from cells within the initial position of the cylinder begins to drop. The uncertainty in the front speed $\boldsymbol{v_{fr}}$ is determined through the uncertainty in the linear fit of the measured position versus time data beyond the induction time $\boldsymbol{\tau^*}$; the uncertainty in $\boldsymbol{\tau^*}$ itself is given by the temporal resolution of the imaging. In all cases, the error bars associated with the uncertainty in the measurements are smaller than the symbol size.

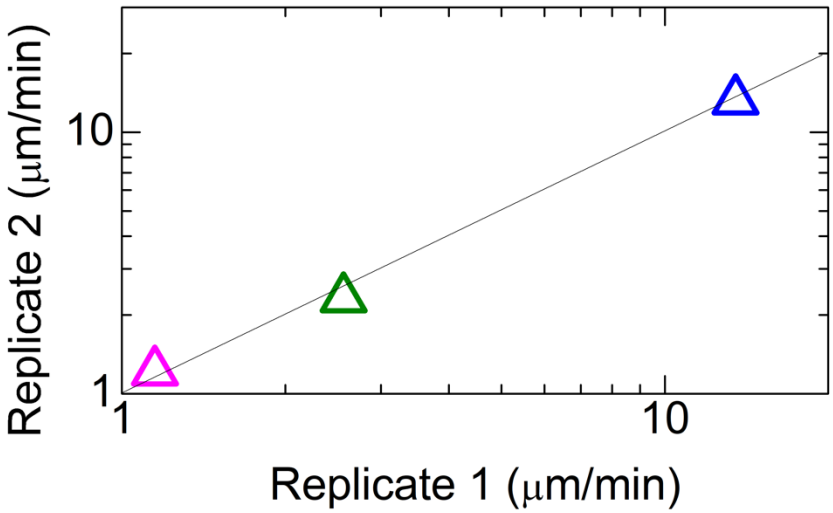

Figure S4: Dynamics of front propagation are reproducible. To confirm the reproducibility of our findings, we perform replicate experiments for each pore size tested. As in the experiments described in Figs. 1-2, we 3D-print a ~1 cm-long cylinder of densely-packed *E. coli* in each medium and visualize the subsequent cellular dynamics. In each experiment, we again find that coherent fronts of cells form and propagate outward. Moreover, by tracking the position of the leading edge of the front over time, we determine the front speed $\boldsymbol{v_{fr}}$, and find excellent quantitative agreement between the results shown in Figs. 1-2 ("Replicate 1") and the replicate experiments ("Replicate 2"). For the Replicate 2 experiments we image the central plane of the 3D printed bacterial colonies, collecting data from an optical thickness of 78.5 μm. We track the position of the leading edge of the wave by setting an intensity cutoff above the noise floor (0.1-1% of initial population intensity or 1-5% of peak intensity after wave formation). Average front locations are identified from three different intensity cutoff (by varying them by +/- 10%). Beyond the induction time, we extract the speed of the chemotactic front by measuring the slope of the average position vs time data.

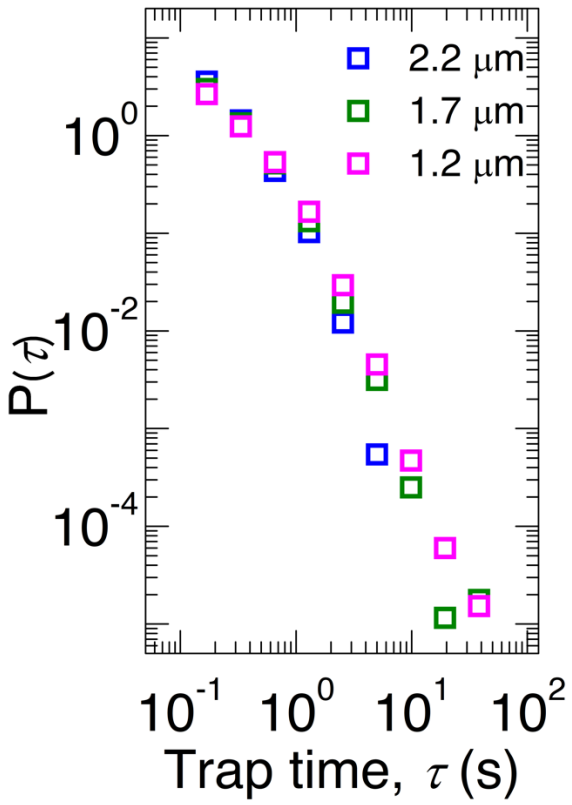

Figure S5: Trapping duration distributions of cells at the leading edge of the front. We track individual cells at the leading edge of propagating fronts measured in media with three different mean pore sizes, indicated by the legend. The cells exhibit hopping-and-trapping motility; similar to isolated cells in gradient-free media, the probability density of trapping durations exhibits a power-law tail. Notably, the majority of trapping durations is smaller than the mean chemotactic memory time of *E. coli*, ~4 s. The three distributions represent three separate experiments, one in each medium of a different pore size; in each experiment, we track hundreds of cell trajectories (between 170 and 280) from time-lapse images captured at 5-12 different locations along the leading edge of each propagating front. Altogether, these data represent the statistics for between approximately 600-2300 hopping and 1700-6800 trapping events for each medium.

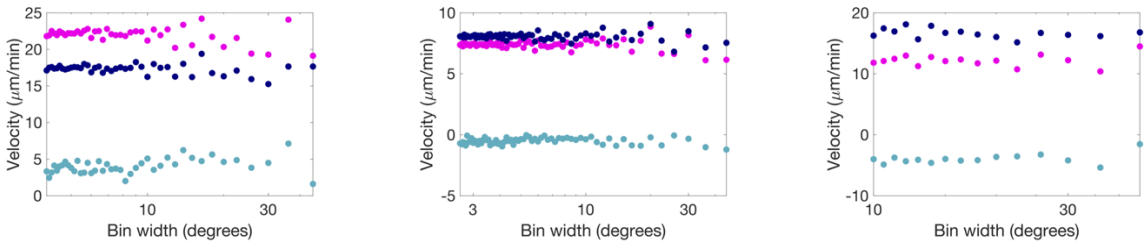

Figure S6: Bias in hopping orientation is the primary contributor to chemotactic migration. Plots show migration velocity calculated using the discrete sum version Eq. 1 of the main text, as described in the *Methods* text section "connecting single-cell motility to front propagation", incorporating all factors (magenta), replacing orientation-dependent hopping lengths with the mean (dark blue) or replacing orientation-dependent hopping probability with a uniform distribution (teal). From left to right, data for the largest, intermediate, and smallest pore sizes are shown for different choices of the bin width, showing that the result reported in Fig. 3 is not sensitive to the choice of bin width. The data show that removing the bias in hopping orientation makes the largest difference in the calculated migration velocity for all pore sizes—that is, the bias in hopping orientation is the primary contributor to chemotactic migration.

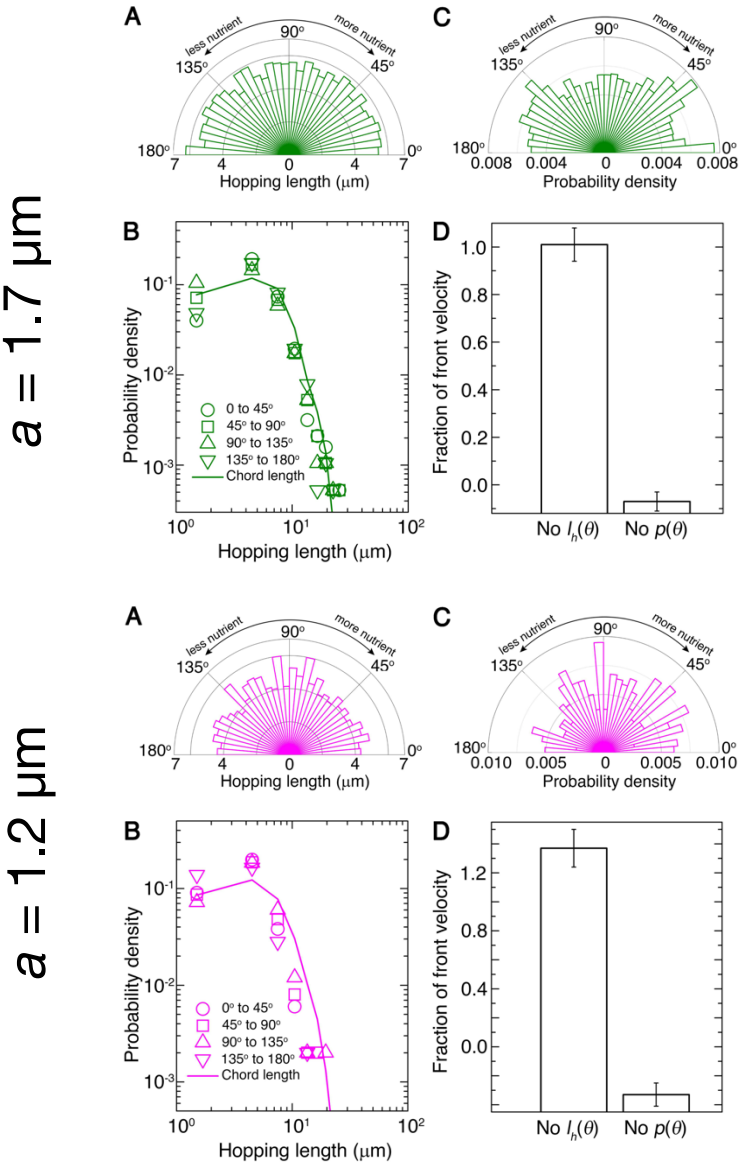

Figure S7: Biased motion of single cells in medium- and small-pore media. (A) Mean lengths of hops along different orientations $|\boldsymbol{\theta}|$ with respect to the propagation direction. **(B)** Symbols show probability density of hopping lengths along different orientations within the ranges indicated by the legend; curve shows measured chord length distribution function for the porous medium. **(C)** Probability density of hopping along different orientations. We consistently observe a slight directional bias: the bars are longer, indicating more hops, for orientations along the direction of front propagation, $\mathbf{0} \leq |\boldsymbol{\theta}| \leq \mathbf{90}^\circ$. In particular, 51.6% and 52.2% of hops have an angle between $[\mathbf{0}, \mathbf{90}^\circ)$ while only 48.1% and 46.9% have an angle between $(\mathbf{90}^\circ, \mathbf{180}^\circ]$ in media with a = 1.7 and 1.2 μm, respectively; the remaining 0.3% and 0.9%, respectively, occur at $\mathbf{90}^\circ$. **(D)** Chemotactic migration velocity calculated using Eq. 1, replacing orientation-dependent hopping lengths with the mean (first bar) or replacing orientation-dependent hopping probability with a uniform distribution (second bar). The second bar is slightly negative, indicating that measured hop lengths are on average slightly larger opposite the propagation direction–likely due to limited statistics. That front propagation would halt entirely or reverse without a bias in hopping orientation demonstrates that this bias is the primary driver of chemotactic migration. Error bars show standard deviation of velocity calculated using different angle bin widths.

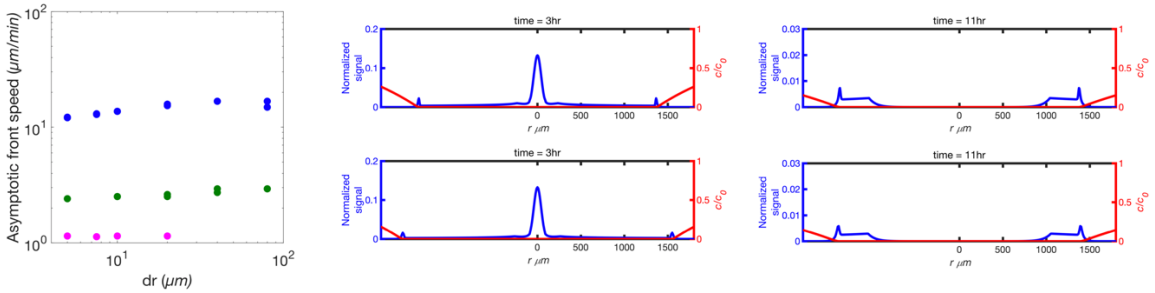

Figure S8: Choice of discretization in numerical simulations does not influence results. (Left panel) Long-time front speed for simulations representing chemotactic migration in porous media with a = 2.2, 1.7, and 1.2 μm (blue, green, magenta, respectively). We use two values of temporal discretization dt for each value of spatial discretization dr to ensure a sufficient time resolution was chosen; top and bottom rows show dr = 5 and 10 μm and dt = 0.001 and 0.01 s, respectively. Simulations showing normalized cell signal (blue) and normalized nutrient concentration (red) for a = 2.2 and 1.7 μm (**middle** and **right** panels, respectively) show minimal variation between choices of discretization indicated.

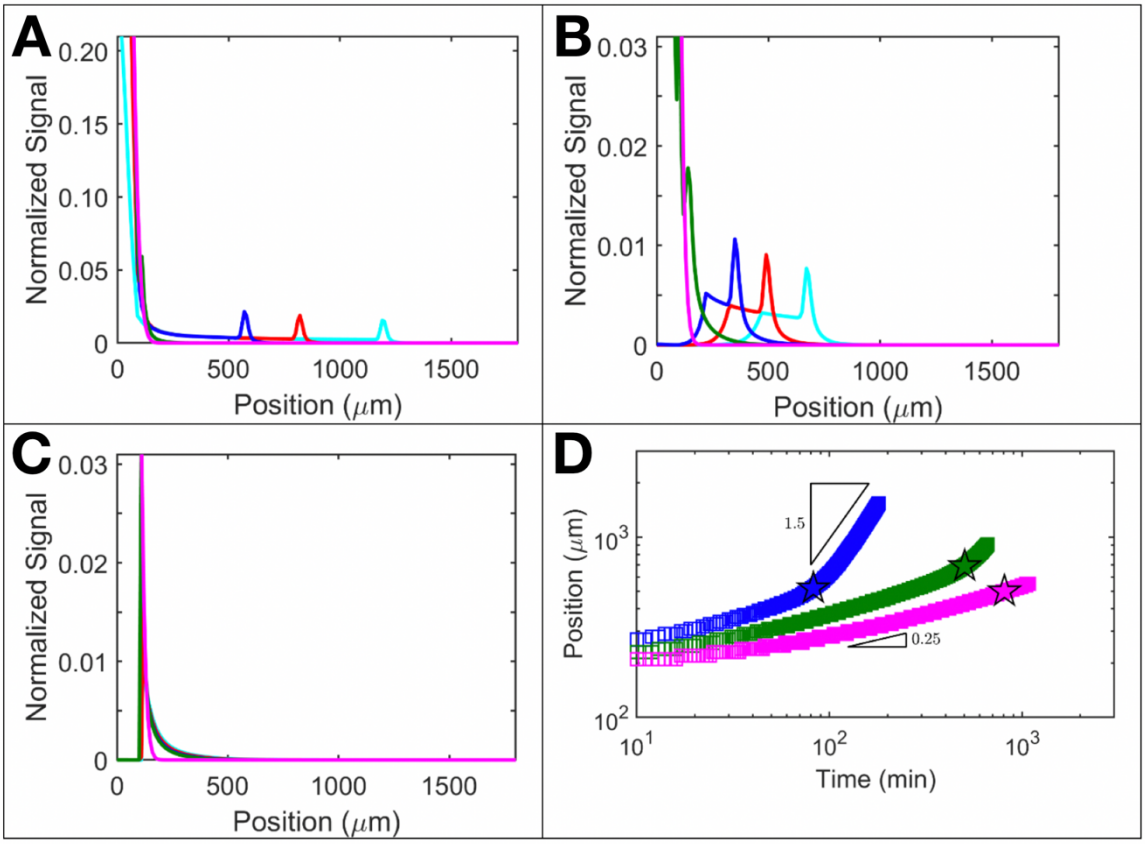

Figure S9: In the absence of growth, fronts still form and propagate, but are hindered in a confinement-dependent manner. Additional simulations of chemotactic migration without bacterial growth; panels **A-C** correspond to the same simulations as in Fig. 4A-C, but with γ=0; colors correspond to the same times as in Fig. 4A-C. In the media with largest pores (A), front propagation appears to be similar to the case of non-zero growth, indicating that chemotaxis plays a dominant role in driving front propagation in these media; compare panel A to Fig. 4A. In the media with intermediate sized pores (B), front propagation is slower without growth; compare panel B to Fig. 4B. In the media with smallest pores (C), propagating fronts do not appreciably form over the simulation time scale, indicating that growth plays a dominant role in driving front propagation in these media; compare panel C to Fig. 4C. The resultant dynamics of the position of the leading edge of the front are shown in **(D)**.

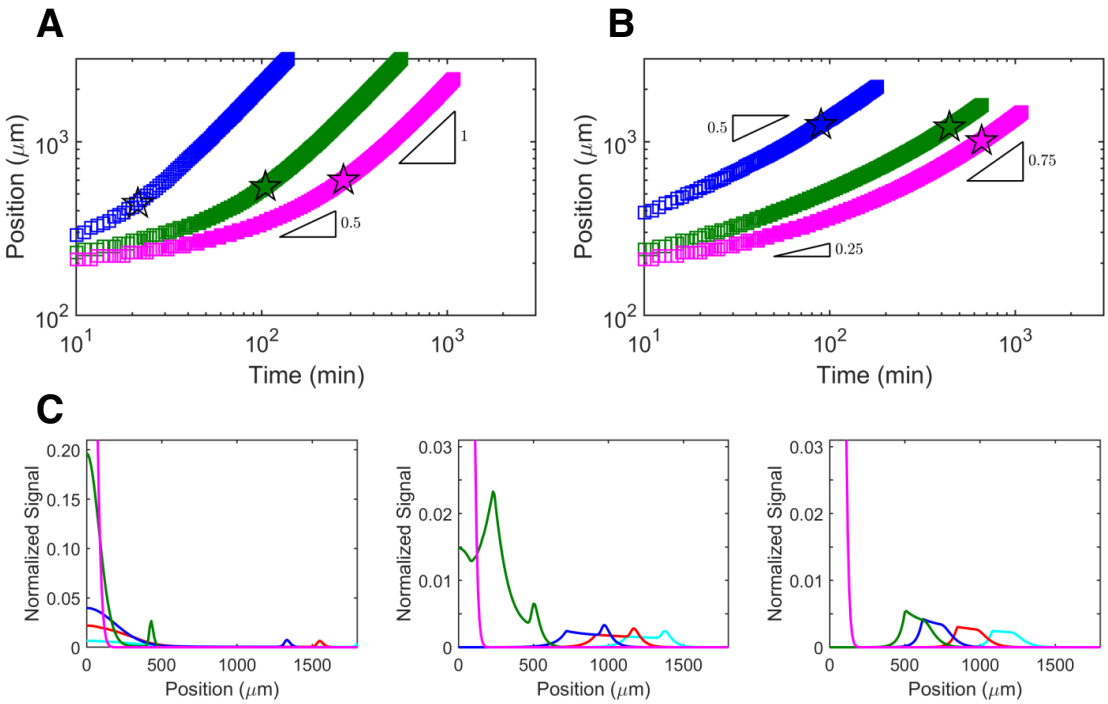

Figure S10: Further simulations of front propagation. (A) Front propagation in rectilinear coordinates. Leading-edge position r motion of the propagating front over time t for simulations performed in rectilinear coordinates; colors correspond to those in Fig. 4. Stars indicate the crossover from slower to faster $r \sim t$ motion. In this case, we observe closer agreement to the crossover from slower to faster $r \sim t$ motion observed in the experiments than simulations performed in cylindrical coordinates. We conjecture that this agreement reflects the influence of boundaries in the experiment: while the experiments initially have cylindrical symmetry, with the initial 3D-printed cylinder placed far from all boundaries, as fronts propagate, they begin to approach the bottom boundary of the imaging chamber. Specifically, the simulations indicate that the region of nutrient depletion reaches the bottom boundary after ~0.5-1 h; in this case, the symmetry of the fronts is no longer cylindrical in the experiments, but has a rectilinear component. **(B)** Without collisions, simulations do not exhibit the transition to $r \sim t$ motion observed in the experiments. To assess the importance of cell-cell collisions in the model, we perform the same simulations as in Fig. 4, but without the corrections to the motility parameters that incorporate cell-cell collisions; colors correspond to those in Fig. 4. We fit the chemotactic parameter such that the speed over the last 30 minutes of the simulation matches the experiment, similar to our method for the main text, except here we impose no effects of cell-cell collisions. The values of chemotactic parameter obtained are 10, 0.9, and 0 $\mu m^2/s$ for the pore sizes in decreasing order, notably smaller than the values obtained by considering collisions. Moreover, none of the simulations achieve ballistic scaling in the absence of collisions. We note that for the case of χ_0 = 0 $\mu m^2/s$, propagating fronts still occur—in this case, however, driven by cellular growth. In particular, nutrient diffusing inward to the leading edge of the population enables continual growth, driving outward spreading. **(C)** Profiles of simulated cellular signal, normalized by maximal initial value, for different radial positions and at different times, for simulations in panel B. Left to right panels show results for media with a = 2.2, 1.7, and 1.2 μm, respectively; colors show different times as indicated in Fig. 4. Without cell-cell collisions, the simulated front profiles have different shapes from the experiments. In particular, the peak heights are further reduced, and for the smallest pore size, the peak of the front is not at its leading edge but rather is toward the back — again highlighting that cell-cell collisions arising from crowding are necessary for an improved agreement with the experiments.

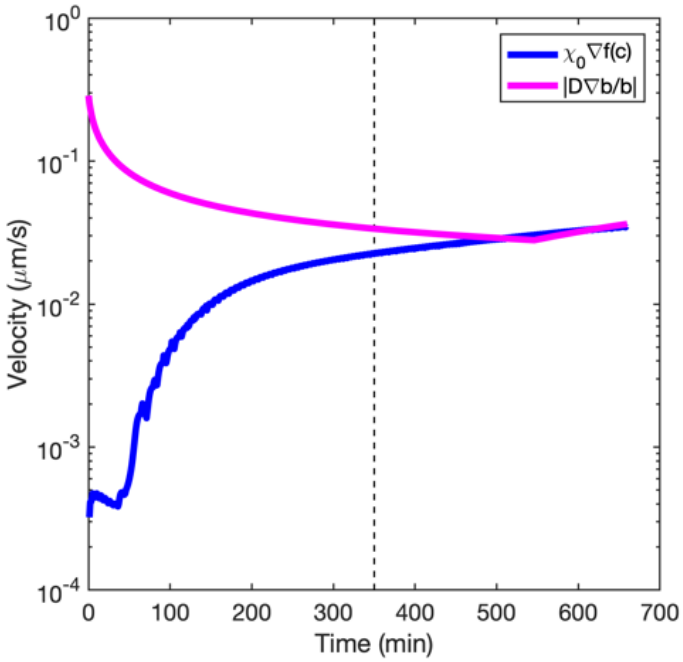

Figure S11: Simulations shed light on the physics underlying the observed transition in front dynamics. An example for the case of intermediate pore-size media shows the variation of the maximum local chemotactic velocity (blue) and maximum local diffusive velocity (magenta) over time. At early times, the cell gradient is steep due to the sharp boundary of cells in the initial geometry of the population. This steep cell gradient drives diffusive flux, but decreases with time, as shown by the magenta curve. Meanwhile, chemotaxis begins low because (i) consumption must first reduce nutrient to within sensing levels and (ii) collisions halt the chemotactic response of cells within the dense starting region. Then, as the population spreads out, the chemotactic flux increases, and at the induction time (dashed line), the two velocities become comparable and eventually reach a steady state. We note that the diffusive process considered here is not thermal diffusion—which our previous experiments using non-motile cells established to be negligible for these conditions (Ref. 14)—but is active diffusion arising from the random walks performed by motile cells as they "hop" through the pore space, punctuated by transient "traps".